Energy confinement and MHD activity in shaped TCV plasmas with localized electron cyclotron heating

A. Pochelon, T.P. Goodman, M. Henderson, C. Angioni, R. Behn, S. Coda, F. Hofmann, J.-P. Hogge, N. Kirneva[a], A.A. Martynov[a], J.-M. Moret, Z.A. Pietrzyk, F. Porcelli[b], H. Reimerdes, J. Rommers, E. Rossi[b], O. Sauter, M.Q. Tran, H. Weisen, S. Alberti, S. Barry, P. Blanchard, P. Bosshard, R. Chavan, B.P. Duval, Y.V. Esipchuck[a], D. Fasel, A. Favre, S. Franke, I. Furno, P. Gorgerat, P.-F. Isoz, B. Joye, J.B. Lister, X. Llobet, J.-C. Magnin, P. Mandrin, A. Manini, B. Marlétaz, P. Marmillod, Y. Martin, J.-M. Mayor, J. Mlynar, C. Nieswand, P.J. Paris, A. Perez, R.A. Pitts, K.A. Razumova[a], A. Refke, E. Scavino, A. Sushkov[a], G. Tonetti, F. Troyon, W. Van Toledo, P. Vyas

Centre de recherches en physique des plasmas,
Association Euratom – Confédération suisse,
Ecole polytechnique fédérale de Lausanne,
Lausanne, Switzerland

[a] Institute of Nuclear Fusion, Russian Research Center, Kurchatov Institute, Moscow, Russian Federation

[b] Istituto Nazionale Fisica della Materia e Dipartimento di Energetica, Politecnico di Torino, Turin, Italy

Abstract. Confinement in TCV electron cyclotron heated discharges was studied as a function of plasma shape, i.e. as a function of elongation, $1.1 < \kappa < 2.15$, and triangularity, $-0.65 \leq \delta \leq 0.55$. The electron energy confinement time was found to increase with elongation, owing in part to the increase of plasma current with elongation. The beneficial effect of negative triangularities was most effective at low power and tended to decrease at the higher powers used. The large variety of sawtooth types observed in TCV for different power deposition locations, from on-axis to the $q = 1$ region, was simulated with a model that included local power deposition, a growing $m/n = 1$ island (convection and reconnection), plasma rotation and finite heat diffusivity across flux surfaces. Furthermore, a model with local magnetic shear reproduced the experimental observation that the sawtooth period is at a maximum when the heating is close to the $q = 1$ surface.

1. Introduction

The improvement in tokamak performance over the last 25 years is not only due to the fact that tokamaks have grown in size, but is also a result of modifications of the basic tokamak concept. The evolution from circular to non-circular cross-sections and, in particular, the vertical elongation of the plasma cross-section, κ, allows for higher plasma current, since the maximum current scales typically as $I_p \propto (\kappa^2 + 1)/2$.

Increasing the plasma current offers two advantages. The first advantage is that the global energy confinement time increases nearly linearly with current, according to several widely used scaling laws, in L confinement mode as well as in H mode [1–3]. The second advantage is that vertically elongated and D shaped cross-sections allow much higher normalized pressures, i.e. β values, than circular cross-sections [4, 5]. The β limit, determined from numerical MHD stability analysis [5], $\beta = c_T I_p/aB$, with β in per cent, scales with the plasma current I_p (MA); a (m) is the minor radius, B (T) is the toroidal magnetic field and c_T is the Troyon factor, which is typically between 2.5 and 4.0, depending on the pressure and current profiles. The good agreement of ideal β limit calculations in highly elongated

plasmas with experiment [6, 7] strongly suggests increasing the design κ in ITER.

At present, ECH experiments [8, 9] on TCV (achieved parameters: $R = 0.89$ m, $a = 0.25$ m, $\kappa = 2.58$, $-0.7 < \delta < 0.9$, $I_p = 1$ MA, $B = 1.43$ T) are aimed at the study of the confinement properties of variably shaped plasmas. In these experiments, an ECH power of 1.4 MW is injected at the second harmonic, 82.7 GHz. This power level is already an order of magnitude larger than the ohmic power during ECH, but represents only a third of the planned total power (3 MW at the second harmonic and 1.5 MW at the third harmonic, 118 GHz). ECH has been chosen for TCV to cope with the large variety of plasma shapes. Each 0.5 MW gyrotron is connected to a steerable launcher, which can be moved during a tokamak discharge. A universal polarizer is included in each transmission line to provide the polarization needed at the plasma boundary for optimal power coupling.

A number of improvements were made to the first wall graphite protection during the 1997 shutdown. Surface coverage was increased from ∼60 to ∼90% by addition of new tiles on previously exposed areas on the low field side wall. These new elements now allow for heating of negative triangularity discharges. The central column tiles were completely redesigned and now have a toroidal profile optimized for high power experiments. The wall is boronized regularly.

2. Confinement as a function of plasma shape

2.1. Confinement study: Definition and parameter range

The aim is to study confinement as a function of elongation κ ($1.1 < \kappa < 2.15$) and triangularity δ ($-0.65 < \delta < 0.55$), with values of both parameters being defined at the edge. Two values of the engineering safety factor q_{eng} ($q_{eng} = 5abB/RI_p$), 1.7 and 3, are used ($2.3 < q_a < 6$; $0.2 < I_p < 0.7$ MA); q_{eng} is used instead of the usual q_a to parametrize the plasma current since constant q_{eng} results in similar normalized profiles independent of the plasma shape [10]. The standard central density n_{e0} is $\sim(2\text{–}2.5)\times10^{19}$ m^{-3}, while the influence of density is only studied for a restricted number of shapes. All discharges are limited L mode discharges. Up to 1.4 MW ECRH was injected, with the power deposition region located near the magnetic axis, largely

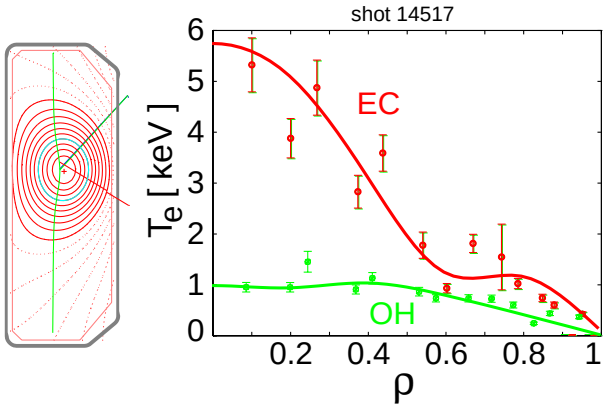

Figure 1. Thomson electron temperature profile for $\kappa = 1.5$, $\delta = 0.2$, $n_{e0} = 1.3 \times 10^{19}$ m^{-3} during ohmic heating and ECRH (1.4 MW). The central deposition, inside the $q = 1$ surface (in blue), is targeted with upper lateral and equatorial beams.

inside the sawtooth inversion radius. At higher q_{eng}, owing to the finite beam width and shrinking of the $q = 1$ surface, together with a smaller paramagnetic resonance shift at lower current, the beam moves somewhat off-axis, but is still well inside the $q = 1$ radius. Thus, we always have central power deposition conditions.

Three gyrotrons were used for this study, two of them launching from the upper lateral ports and one from the equatorial port. The power was raised to its maximum value in three steps of typically 0.2 s duration. Confinement data are used after the establishment of a constant soft X ray flux; this condition led to the exclusion of a 40–50 ms transient period at the start of each power step. Between the second and third steps the power was modulated for 0.2 s. The power deposition location was obtained from soft X rays at the ECH shut-off [11], from power modulation experiments and qualitatively from the sawtooth shapes (Section 3.1).

The ECH power P_{ECH} can be measured near the torus calorimetrically between discharges. The gyrotron power can be set within 5% and is indeterminate to ±10%.

The electron energy content W_{Ee} is obtained from Thomson scattering measurements, taken every 17 ms. The T_e and n_e profiles, measured along a vertical chord (at $R = 0.9$ m), are projected on to normalized flux co-ordinates and fitted with cubic splines. Therefore, the calculation of W_{Ee} depends on the equilibrium reconstruction and on the profile fits. This procedure is straightforward for positive triangularity and low elongation discharges, where

MHD mode activity is low, as for the case of the discharge shown in Fig. 1. For negative triangularity and high elongation, the profiles show occasionally large fluctuations within the sawtooth inversion radius, which can make the fitting procedure problematic. Such shots had so far to be rejected from the database. The electron energy sometimes fluctuates strongly in time owing to large sawtooth relaxations at positive triangularity and with 1.4 MW of ECRH. Typically, ten Thomson profiles were available after the exclusion of the initial transient period at the beginning of each step. These multiple profiles were averaged to reduce the influence of fluctuations.

Typical values of the effective charge Z_{eff}, calculated from soft X ray flux (dominated by carbon emission) and Thomson temperatures, are $Z_{eff} \geq 4$ during the ohmic heating and ECRH phases. Bulk ion temperatures from neutral particle analysis range from 200 to 250 eV. Therefore, the ion contribution to the total energy is negligible.

2.2. MHD activity

MHD activity not only influences the T_e profile reconstruction but can also degrade the confinement itself. In particular, for $\delta < -0.2$ the $m/n = 2/1$ mode has been frequently observed during phases with and without auxiliary heating power and irrespective of the edge safety factor.

Sawteeth were present in a wide range of the investigated plasma shapes. Ohmic sawteeth, at $\kappa = 1.5$, $\delta = 0.2$ and typical densities of $(2-3) \times 10^{19}$ m^{-3}, have a period $\tau_{ST} \approx 2$ ms. Their period and size increase with triangularity up to $\tau_{ST} \approx 3$ ms and up to a relative crash amplitude of 20% observed with a soft X ray diode viewing the plasma core (I_{SXR}). For negative δ the relative crash amplitude decreases to a few per cent and can disappear within the resolution limit [12]. The crash amplitude as well as the sawtooth period decreases with increasing elongation. Occasionally, no sawteeth have been observed in discharges with $\kappa > 2$.

With the addition of ECH, deposited within the $q = 1$ surface, different forms of sawteeth have been observed, ranging from normal triangular sawteeth for on-axis deposition to saturated and inverted sawteeth for deposition closer to the inversion radius. For $q_{eng} = 2$, $\kappa = 1.5$, $\delta = 0.2$, the observed sawtooth shapes change with increasing heating power from normal to saturated to inverted. For a higher value of $q_{eng} = 3$, and therefore with a reduced inversion radius, saturated sawteeth already appear at lower heating power, indicating that the actual deposition was somewhat further off-axis, closer to the inversion surface (Section 3.1.1).

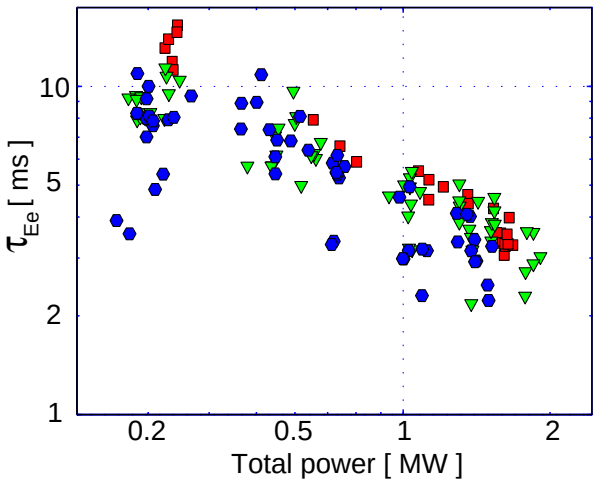

Figure 2. Electron confinement time versus total power for $\kappa = 1.5$, $\delta = 0.2$ (red squares, $n_{e019} > 3$; green triangles, $2 < n_{e019} < 3$; blue hexagons, $n_{e019} < 2$).

The effect of power on sawtooth period and size indicates a strong triangularity dependence: for instance, at moderate elongation $\kappa \approx 1.5$, for small positive triangularity $\delta > 0.2$ and at low q_{eng} to ensure central deposition, the sawtooth period and crash amplitude increase with heating power up to $\tau_{ST} \approx 5$ ms and up to a relative crash amplitude of 35%, whereas for $\delta < 0.2$ the sawtooth period decreases with increasing heating power, with smaller crash amplitude. Therefore, with increasing power, positive triangularity shows a sawtooth stabilization effect, but associated with large crash amplitudes; in contrast, increasing power in negative triangularity discharges induces sawtooth destabilization and smaller crash amplitudes, which can be of advantage in schemes trying to avoid seed island formation.

2.3. Scaling of electron energy confinement time

The dependence of the electron energy confinement time on total power and density was studied over a wide power range for the different plasma shapes and in particular in the centre of the (κ, δ) scan ($\kappa = 1.5$, $\delta = 0.2$), as shown in Fig. 2. The electron energy confinement time τ_{Ee} is clearly seen to decrease with power and to increase with density.

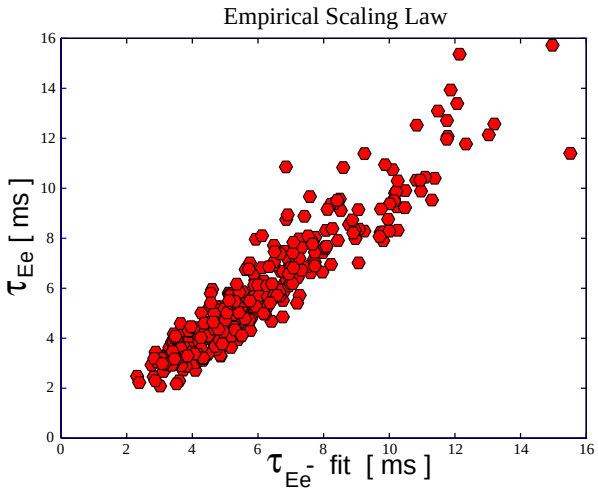

Figure 3. Empirical scaling law (Eq. (1)) for the TCV ECRH data set in the case of $\alpha_I = 0.5$.

In an attempt to obtain a simple general power law to describe the dependence of τ_{Ee} (ms) on average line density n_{eav} (in units of 10^{19} m^{-3}), total power P (MW), edge elongation κ, edge triangularity δ and plasma current I_p (MA), we applied a multivariable regression to the database. The dependences on κ and I_p cannot be separately determined, owing to the strong correlation between these quantities in our data set. The power law expression must therefore contain a free parameter, as follows:

$$\tau_{Ee} = 2 \times 6^{\alpha_I} n_{eav19}^{\alpha_n} P^{\alpha_P} I_P^{\alpha_I} \kappa^{\alpha_\kappa} (1+\delta)^{\alpha_\delta} \qquad (1)$$

where $\alpha_n = 0.46 \pm 0.2$, $\alpha_P = -0.7 \pm 0.1$, $\alpha_\kappa = 1.4(1-\alpha_I) \pm 0.4$, $\alpha_\delta = -0.35 \pm 0.3$ and α_I remains undetermined. These uncertainties result from a 25% error on τ_{Ee}. Good fits are obtained with α_I in the range $0 \leq \alpha_I < 0.7$, as illustrated in Fig. 3 for the case $\alpha_I = 0.5$.

If instead of the above five variable regression a four variable regression is used, with no explicit current dependence ($\alpha_I = 0$), a very favourable elongation power exponent, $\alpha_\kappa \approx 1.4$, is obtained, indicating the good overall effect of elongation, with the determination of the separate contributions of elongation and plasma current being ignored. In fact, further data at moderate elongation are needed to reduce the strong correlation of plasma current and elongation in the present database. However, the main reason for developing elongated discharges is to increase the plasma current. At high elongation, low current operation is limited by vertical stability, in ohmically heated discharges and in the present central deposition ECRH cases. Therefore, broadening

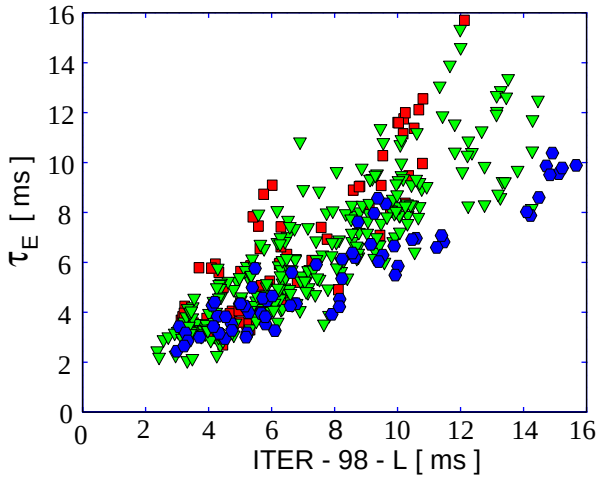

Figure 4. Fit to the ITER-98-L mode scaling law. Since triangularity does not appear in ITER-98-L, it is explicitly indicated by the symbols: negative δ appears favourable (red squares, $\delta < 0$; green triangles, $0 < \delta < 0.3$; blue hexagons, $\delta > 0.3$).

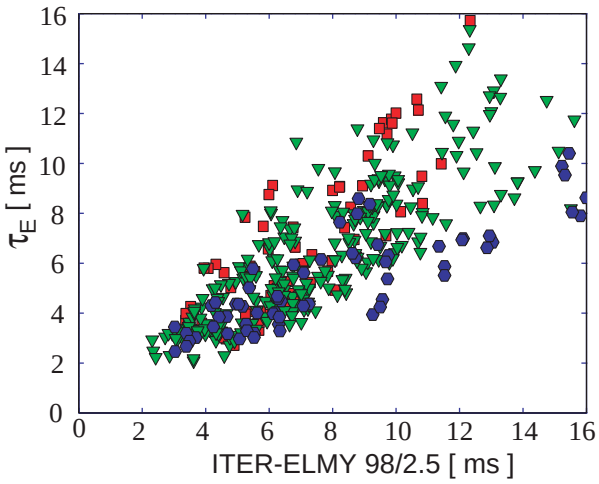

Figure 5. Fit to the ELMy H mode scaling law with an H factor of 2.5 [3] (same symbols as in Fig. 4).

of the current profile by proper use of off-axis ECRH or ECCD could also be of help to decorrelate elongation and current by enlarging the range of stable equilibria.

The scaling (1) displays qualitative similarities with recent scaling laws, such as the ITER-98-L mode scaling [2], where $\alpha_n = 0.40$, $\alpha_P = -0.73$, $\alpha_I = 0.96$, $\alpha_\kappa = 0.64$. Clearly, the α_n and α_P exponents are in agreement, within the uncertainties, with our scaling; however, α_κ and α_I are not compatible with our scaling. Plotting our data against ITER-98-L, as shown in Fig. 4, demonstrates the beneficial effect of negative triangularities.

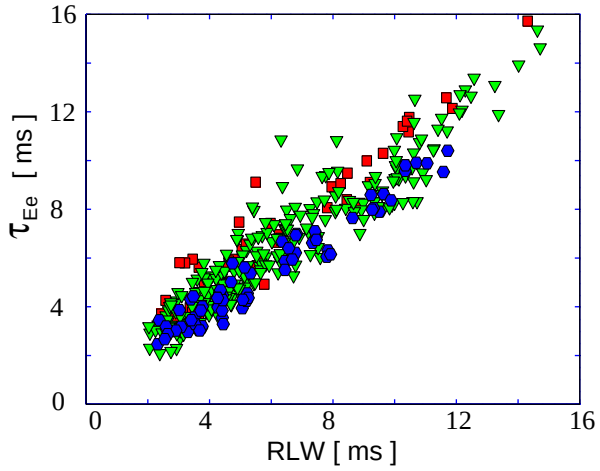

Figure 6. Fit to the Rebut–Lallia–Watkins scaling law: negative δ appears favourable (same symbols as in Fig. 4).

The constraints $\alpha_n = 1/2$ and $\alpha_P = -2/3$ from the ELMy H mode ITER database [3] are also compatible with our scaling. The fit to this ELMy H mode scaling, shown in Fig. 5, indicates again the beneficial effect of negative triangularities.

Naturally, such a general scaling, being based on the entire data set, may overlook more detailed effects in particular regions of the parameter space. For instance, the degradation of confinement with power, when studied discharge by discharge, using the different power steps in one discharge (maintaining constant current and plasma shape), becomes progressively more pronounced as density is increased. Also, the beneficial effect of low triangularity or slightly negative triangularity appears to be stronger at low total power.

Most of the improvement of confinement time with shape changes in ohmic plasmas had been explained earlier in terms of geometrical effects. However, the thermal conductivity of ohmic plasmas was found to be independent of the plasma shape. This observation, combined with geometrical effects on the temperature gradient and degradation with increasing energy flux, was able to explain the observed variation in the energy confinement time [13].

The TCV confinement time is plotted against the Rebut–Lallia–Watkins confinement scaling [14] in Fig. 6 for comparison and shows good agreement. Since the RLW scaling contains no triangularity dependence, the data points have again been subdivided into three triangularity classes; the beneficial effect of negative triangularity is evident, although less visibly than in the scalings of Figs 4 and 5. The best fit is obtained with RLW, but the two others are not far off.

2.4. Transport modelling (PRETOR, ASTRA)

Some of the ECH discharges were simulated using PRETOR [15], a predictive time dependent transport simulation code for tokamaks: it couples a 2-D equilibrium solver with the flux surface averaged 1-D transport equations to compute the evolution of temperature and density of electrons, ions and impurities. The RLW model [14], which is implemented in the code, was modified only in its geometrical dependence to simulate discharges with an edge safety factor larger than 5, as the original model did not allow satisfactory simulations of ohmic TCV discharges in this domain [16]. The experimental temperature profiles of a single shot in the ohmic phase were analysed and the heat conductivity was adjusted to reproduce the experimental behaviour, which implies a relatively large transport at the edge and smaller transport in the centre. The formula for the electron thermal conductivity χ_{RLW} in Ref. [16] was changed to:

$$\chi_{RLW} = \frac{0.45}{R_0^{1/2}}\,\varepsilon^{1/2}\,(1+Z_{eff})^{1/2} \times \left|\left(\frac{\partial_\rho T_e}{T_e} + 2\,\frac{\partial_\rho n_e}{n_e}\right)\frac{q^2}{\partial_\rho q}\right|\left(\frac{T_e}{T_i}\right)^{1/2} B_t^{-1} \times \left(\frac{1}{2}+\frac{\rho}{a}\right)^2\left(1-\frac{(\partial_\rho T_e)_c}{\partial_\rho T_e}\right) H(\partial_\rho T - (\partial_\rho T_e)_c) \quad (2)$$

where $H(x)$ is the Heaviside function, $\partial_\rho = \partial/\partial\rho$ and $(\partial_\rho T_e)_c$ is the electron temperature critical gradient.

With this model, keeping the free parameter fixed in all the transport coefficients, discharges were simulated in the ohmic heating and ECH phases. A satisfactory agreement is obtained for the temperature (Fig. 7(a)) and density profiles (Fig. 7(b)), the electron thermal energy and the confinement time, assuming total absorption for the different ECH powers injected. In some ECH discharges a 'pump-out' effect is observed between sawtooth crashes, which implies that the local particle transport coefficients should be modified in the centre. This has not yet been included in PRETOR but is not significant with respect to the confinement time.

Simulations of the same discharge were performed with ASTRA, a transport code based on the canonical transport model [17], which is a model of

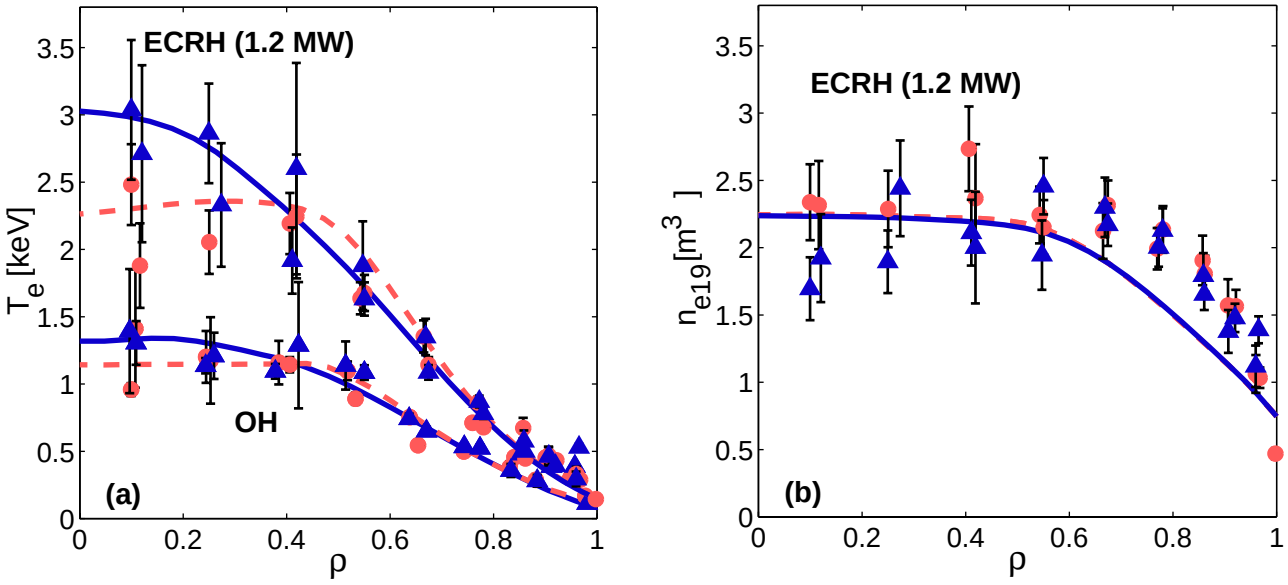

Figure 7. Comparison between simulated PRETOR profiles and TCV experimental profiles for (a) temperature and (b) density in ohmic heating and ECRH (1.2 MW) discharges, before (blue solid line and triangles) and after (red dashed line and solid circles) sawtooth crash ($\kappa = 1.8$, $\delta = 0.2$, $n_{e0} = 2.3 \times 10^{19}$ m^{-3}, $q \approx 5$). Owing to central pump-out with central power deposition, the experimental density profile becomes hollow in such a shot and fills in at each sawtooth crash; the ohmic density profile (not shown) is close to the post-crash ECRH profile.

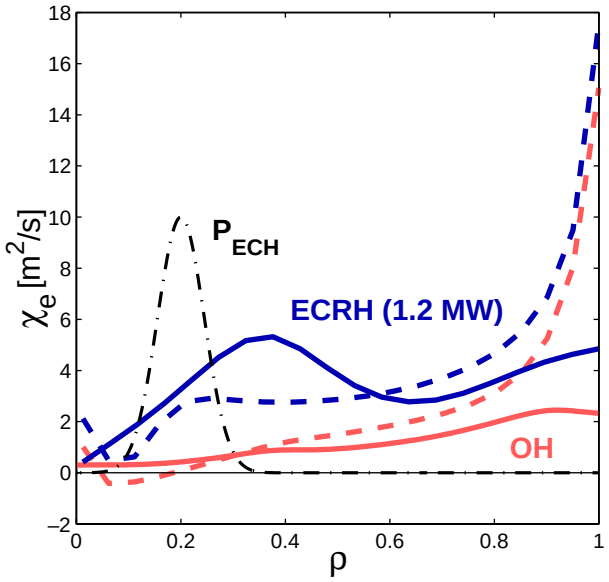

Figure 8. Comparison between PRETOR (solid lines) and ASTRA (dashed lines) χ_e profiles in ohmic heating (red lines) and ECRH discharges (blue lines). The chain line indicates the ECH power deposition profile (in arbitrary units).

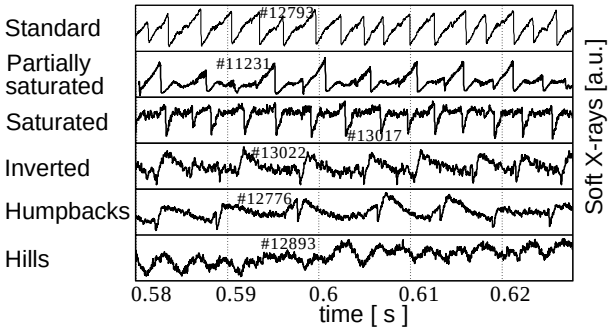

Figure 9. Standard sequence of central relaxations obtained when moving deposition from the magnetic axis (top) to the inversion radius (bottom). Standard sawteeth are produced by on-axis power deposition, and humpbacks and hills by deposition close to the inversion radius.

self-consistent profiles including a heat pinch. In these simulations, good agreement was also found with temperature profiles and confinement time.

With a measured ratio of $P_{rad}/P_{OH} \approx 0.2$, using the radiated power measured from bolometry, one must assume 90% absorption of injected power, which is within the error bar of the power measurement. A higher radiation level, around $P_{rad}/P_{OH} \approx 0.3$, would be consistent with full power absorption. Thus, our data can satisfactorily be simulated by both transport codes.

Comparing the heat diffusivities χ_e obtained from the ASTRA and PRETOR codes in Fig. 8, we

observe that: (1) ASTRA shows a larger transport enhancement close to the edge; (2) there is good agreement in the intermediate region, $0.5 < \rho < 0.8$, with χ_e in ASTRA higher than in PRETOR by about 20% for ECRH and by a factor of 2 for ohmic heating; (3) inside $\rho = 0.5$, ASTRA shows the effect of heat pinch, which can allow for inward total heat fluxes at the centre. On the other hand, PRETOR shows a consistent enhancement of the anomalous transport close to the ECRH power deposition location caused by the presence of steeper temperature gradients.

3. Simulation of central relaxations with localized power deposition

3.1. Central relaxation shape modelling

3.1.1. Experimental description

Non-standard sawtooth traces have been observed in TCV during intense localized ECH [18, 19]. Figure 9 shows a sequence of soft X ray traces obtained while varying the ECH deposition radius. With on-axis deposition, standard, i.e. triangular, sawteeth are observed. However, as the ECH absorption region is moved off-axis, the soft X ray traces change their shape: partially saturated and saturated sawteeth are observed when the heating is still within the $q = 1$ radius. Interestingly, the precursor oscillations that precede the fast relaxation phase of a saturated sawtooth sometimes double their frequency [20]. Humpback sawteeth, first reported by the T-10 team [21, 22], are observed in TCV when the heat is deposited close to the inversion radius. For slightly larger deposition radii, the soft X ray traces acquire hill-like shapes of low amplitude. Another intriguing experimental observation concerns the optimal deposition radius for obtaining high central temperatures: this radius appears to be often close to the $q = 1$ radius. In fact, the sawtooth or humpback period is longest in this case, and the confinement time is as large as for central deposition.

3.1.2. Model of a growing island under localized heating and diffusion

A theoretical model which accounts for many of the observed features has been recently developed [23]. The model is based on the combined effects of $m/n = 1$ magnetic island dynamics, localized ECH, finite heat diffusivity across the magnetic field lines and plasma rotation. According to this model, the

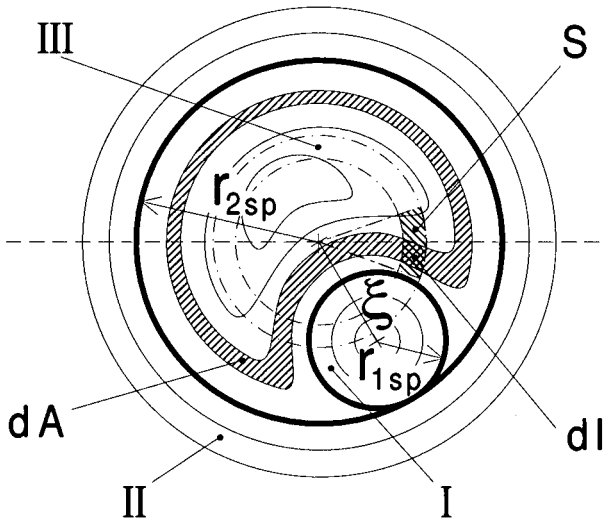

Figure 10. Heat deposition and distribution in a growing and rotating $m = 1$ island. Regions: I, displaced core, vanishing at full reconnection; II, outer region; III, growing island region with new magnetic axis. The heat deposited in the elemental surface dI of the heat source S spreads over the crescent shaped hatched area by parallel diffusion. The addition of rotation further distributes the heat along other families of flux surfaces.

flux surfaces acquire a distinct $m/n = 1$ topology in the plasma central region, described by a helical flux function, $\psi_*(r, \vartheta - \varphi, \xi(t))$, whose detailed analytic form is given in Ref. [23]. Here, $\xi(t) \approx w(t)/2$ is the displacement of the magnetic axis as a consequence of the excitation of a resistive internal kink mode and $w(t)$ is the $m/n = 1$ magnetic island width. The time evolution of $\xi(t)$ is not predicted theoretically, but can be inferred from the experimental data. The limit $\xi(t) \to \rho_{mix}$, with ρ_{mix} the Kadomtsev mixing radius [24], corresponds to full reconnection. Nevertheless, the model is applicable as well to cases of partial sawtooth reconnection.

An example of $\psi_* = $ const contour lines for a given $\xi(t)$ is shown in Fig. 10. The deposited thermal energy spreads rapidly and uniformly on flux surfaces because of the large (practically infinite) parallel thermal conductivity. Rotation distributes the deposited heat on several flux tubes intersecting the ECH absorption region (for the sake of simplicity, we assume rigid toroidal rotation). With reference to Fig. 10, if we denote by dA the cross-sectional area of a generic flux tube and by dI its intersection with the heated region, we can write the ECH power density averaged over flux surfaces as $\langle S \rangle(A) = \rho \partial I/\partial A$, where $\rho = P_{ECH}/V_H$ (= const for simplicity) is

the power density, P_{ECH} is the total ECH absorbed power and V_H is the absorption volume. The thermal energy is transported radially by parallel heat diffusion in a complex magnetic structure such as that of Fig. 10, resulting in an apparently non-local heat transport process.

As a consequence of toroidal flux conservation during the island growth [23, 24] and $B_\varphi \approx$ const, the area bounded by a helical flux surface as this evolves in time is conserved, and thus $A = A(\psi_*)$. Consequently, reconnecting flux tubes mix their thermal energy density (i.e. their pressure) according to the following law:

$$p[A(\psi_*)] = \pi \left(p(r_{2sp}^2)\ \frac{\mathrm{d}r_{2sp}^2}{\mathrm{d}A} - p(r_{1sp}^2)\ \frac{\mathrm{d}r_{1sp}^2}{\mathrm{d}A} \right) \quad (3)$$

where $r_{2sp} - r_{1sp} = \xi(t)$, with r_{1sp} and r_{2sp} the radii of the two circles forming the $m/n = 1$ island separatrix (Fig. 10). These radii, as well as their derivatives with respect to the area, are obtained as a function of the equilibrium helical flux function, $\psi_{*eq}(r^2) \propto \int_0^{r^2} (q^{-1}(r^2) - 1)\ \mathrm{d}r^2$; in particular, since surfaces with equal helical flux reconnect, $\psi_{*eq}(r_{1sp}^2) = \psi_{*eq}(r_{2sp}^2)$. In Eq. (3), we have neglected the magnetic to thermal energy transfer during reconnection, which corresponds to only a few per cent of the ECH thermal energy absorbed in a sawtooth period. The plasma density obeys completely similar relations.

Thus, the temperature evolution is dominated by heating and perpendicular diffusion (a constant $\chi_\perp$ is assumed) in periods during which the $m/n = 1$ magnetic island either is absent or has a stationary width, while convection and mixing due to reconnection become important when the island is growing, the convection pattern being associated with the specific $m/n = 1$ internal kink mode structure. It is convenient to specify the heat transport equation in a Lagrangian frame of reference; thus, $T = T(A, t)$. Taking into account the different topology of the three different regions, I, II and III, indicated in Fig. 10, the diffusion equation takes the form

$$\frac{3}{2}\ \frac{\partial T}{\partial t} = \chi_\perp \left(\langle |\boldsymbol{\nabla} A|^2 \rangle \frac{\partial^2 T}{\partial A^2} + \langle \boldsymbol{\nabla}^2 \mathrm{A} \rangle\ \frac{\partial \mathrm{T}}{\partial \mathrm{A}} \right) + \frac{\langle S \rangle}{n}. \quad (4)$$

In regions I and II, the metric elements simplify: $A = \pi r^2$, with r indicating the distance from the displaced axis in region I. The time evolution of the three regions is specified by the displacement function $\xi(t)$ and by the helical flux function $\psi_*(r, \vartheta - \varphi, \xi(t))$. Equation (4), with appropriate initial and boundary conditions [23], completely specifies our simulation model.

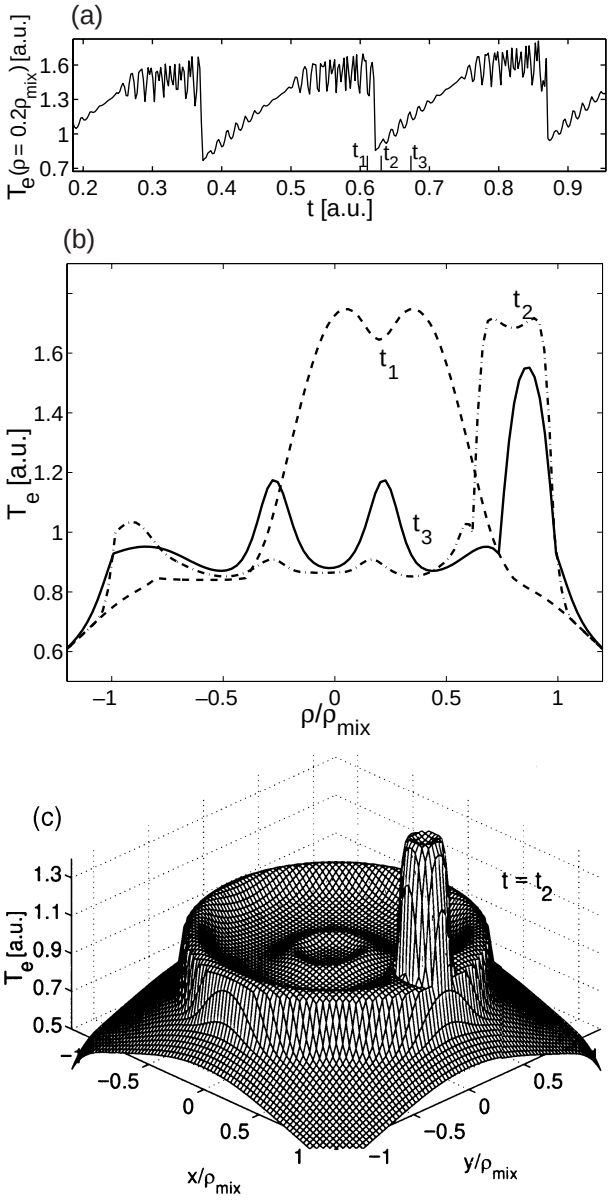

Figure 11. Simulation of partially saturated sawteeth with power deposition between the magnetic axis and the $q = 1$ surface at $\rho = 0.25\rho_{mix}$, with a deposition width of $0.1\rho_{mix}$: (a) temporal evolution of the central temperature (note the appearance of frequency doubling); (b) temperature profile before (t_1) and after crash (t_2, t_3) (see Fig. 11(a)); (c) 3-D temperature profile at time $t = t_2$ after crash.

The model was originally applied to explain the multipeaked temperature profiles and transport barriers observed in high ECH power density experiments such as RTP [25] and TEXT-U [26]. We present below two examples which indicate the

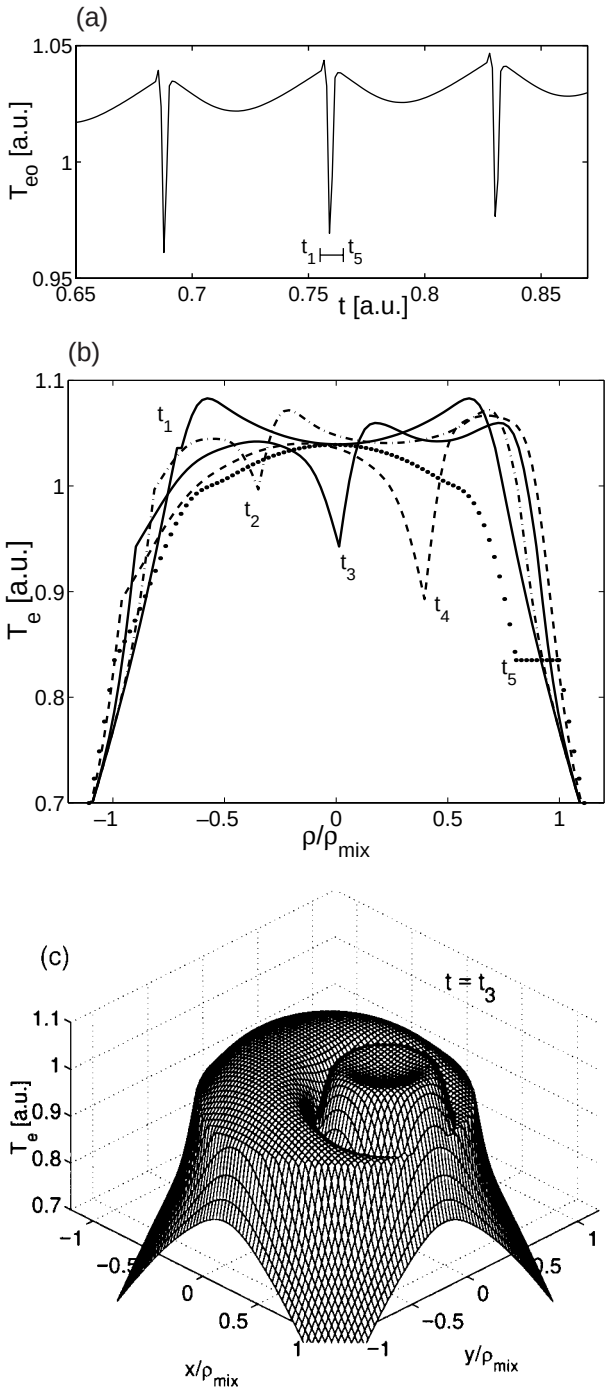

Figure 12. Simulation of humpback sawteeth with power deposition close to the $q = 1$ surface: (a) temporal evolution of the central electron temperature; (b) temperature profile during the fast phase indicated in (a); (c) 3-D temperature profile in the middle of the crash ($t = t_3$).

ability of the model to reproduce the observed sawtooth shapes in TCV.

In the first example (Fig. 11), a saturated sawtooth is simulated. In this simulation, the power deposition region is set to be between about 2 and 4 cm from the equilibrium axis on the high field side; the $q = 1$ radius is at 7 cm. Thus, the heating is off-axis, but is well within the $q = 1$ radius, consistent with the experimental indications. Figure 11(a) shows the simulated temporal trace of the local electron temperature at a distance of about 2 cm from the equilibrium magnetic axis. Frequency doubling appears in the simulation during the evolution of the saturated sawteeth, as is also often seen in the experiment during saturated sawteeth [20]. In Fig. 11(b), three temperature profiles at different phases of the saturated sawtooth are shown. These profiles are non-monotonic within the mixing radius and can become rather spiky. In Fig. 11(c), a simulated 3-D reconstruction of the electron temperature corresponding to the fast relaxation phase at time $t = t_2$ of Fig. 11(a) is shown.

In the second example (Fig. 12), we present the simulation of a humpback sawtooth. In order to obtain a humpback from our model, it is important to place the heating region close to the $q = 1$ radius, for consistency with the experiment. This produces slightly hollow temperature profiles during the quiescent phase, which then become peaked in the centre as a consequence of the growth of the $m = 1$ island. Figure 12(a) shows the temporal evolution of the central electron temperature. Temperature profiles during the fast relaxation phase are shown in Fig. 12(b). The relative minimum in the temperature deepens with time during the fast phase of the humpback relaxation. Indeed, the characteristic signature corresponding to the sudden drop in temperature between the two humps, visible in Fig. 12(a), is related to the fast passage of this relative minimum through the observation point. A 3-D reconstruction of the electron temperature is shown in Fig. 12(c), in which the two hot regions are clearly visible.

For both simulations, the displacement function $\xi(t)$ is assumed to grow rapidly during the observed fast relaxation phase. More specifically, for the case of the simulated saturated sawtooth, $\xi(t)$ grows from $0.2\rho_{mix}$ to $0.8\rho_{mix}$ in about 200 μs; for the humpback sawtooth, $\xi(t)$ grows from practically zero to $0.9\rho_{mix}$ in a similar time interval. These values of $\xi(t)$ are consistent with nearly full reconnection. The typical radial width of the heat deposition region used in the simulations is between 1 and 2 cm. The results are not particularly sensitive to this width when varied within the indicated range. The typical value of the central $\chi_\perp$ used in the simulations is of order 0.1 m^2/s.

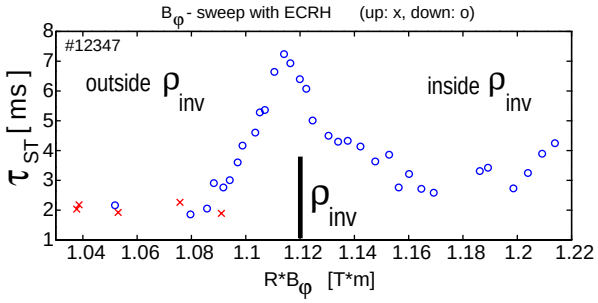

Figure 13. Sawtooth period evolution during a power deposition sweep (toroidal magnetic field sweep). Maximum sawtooth period is observed for deposition close to ρ_{inv}.

Thus, the model successfully reproduces the shapes of different types of central relaxations as the heating radius is varied, at least qualitatively speaking. In addition, consistently with the experiments, the relative amplitude of the relaxations for central versus off-axis deposition is correctly simulated. For example, at constant power injection, high amplitude triangular sawteeth are obtained for on-axis heating, while low amplitude humpback oscillations are obtained when the heating region is close to the $q = 1$ surface.

3.2. Sawtooth period simulation with localized power deposition

The transport code PRETOR (Section 2.4), including a sawtooth model developed previously [27], had been used earlier to simulate sawtooth periods in ohmic discharges of TCV [28]. It is now used to simulate ECRH discharges, since it is known that temperature and density profiles are strongly influenced by the presence (or absence) of sawteeth. In particular, the strong dependence of the sawtooth period on power deposition location observed experimentally (Fig. 13) can also be simulated.

The magnetic shear $s_1 = \rho_1 q'(\rho_1)/q_1$ at $q = 1$ and s_{1crit}, a critical shear above which the resistive internal kink is triggered, define the time at which the sawtooth crash occurs. The sawtooth period depends on the relative temporal evolution of s_1 and s_{1crit}, and therefore mainly on the local plasma parameters. This explains why the sawtooth activity is very sensitive to localized ECRH power deposition, as seen for example in TCV [18, 19]. Indeed, local heating can change both $s_1(t)$, by changing the local resistive time and the current profile, and $s_{1crit}(t)$, by changing the temperature gradients and confinement time. Moreover, localized deposition affects the $q = 1$ radius both in the transport code and in the experiment, as revealed by measurements of the sawtooth inversion radius. We simulated a case with 0.5 MW of ECRH deposited over a radial width of $0.15a$. As the mean deposition radius is changed from $\rho = 0$ to 0.3 to 0.5, the code gives $\rho_1/a = 0.44$, 0.40 and 0.27, respectively. In addition, in the first two cases, s_{1crit} is relatively large (0.35) because heating inside $q = 1$ gives large gradients at $q = 1$. Therefore, long sawtooth periods are obtained, as shown in Fig. 14 ($\rho_{ECRH} = 0.3$). In contrast, heating outside ρ_1 gives a smaller s_{1crit} and therefore shorter sawtooth periods are obtained ($\rho_{ECRH} = 0.4$). This is in qualitative agreement with the experiment, where sawtooth periods of 2 ms are observed when heating outside $q = 1$ and where sawtooth periods are seen to increase rapidly to 7–8 ms when heating approaches the $q = 1$ surface. However, in the experiment, heating closer to the magnetic axis results again in shorter sawtooth periods; this indicates that a more detailed simulation, including the magnetic topology described in Section 3.1.2, is needed when heating inside the reconnecting volume.

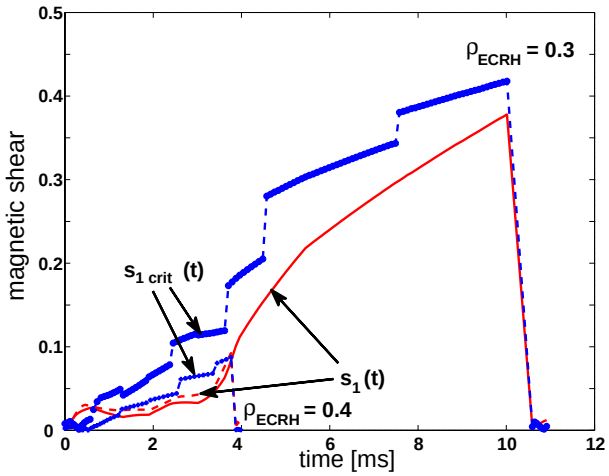

Figure 14. Evolution of the local magnetic shear s_1 (red lines) and critical magnetic shear s_{1crit} (blue lines) for power deposition (1) close to $q = 1$, resulting in a long sawtooth period ($\rho_{ECRH} = 0.3$, solid lines), and (2) outside $q = 1$, resulting in a shorter sawtooth period ($\rho_{ECRH} = 0.4$, dashed lines).

4. Conclusions

The electron energy confinement has been studied as a function of plasma shape, i.e. as a function of elongation and triangularity, in ECH

discharges, with P_{ECH} exceeding P_{OH} by up to an order of magnitude. The electron energy confinement improves with elongation. The beneficial effect of low or negative triangularity on confinement, manifested in ohmically heated plasmas, is also observed in ECH plasmas, but tends to decrease with increasing power. Results of transport simulations, using two different models, are found to be consistent with the experimental data.

Different types of central relaxations (sawteeth) are observed when the location of power deposition is moved from the magnetic axis to the $q = 1$ region. The observed sawtooth shapes have been qualitatively simulated, using a model with localized power deposition, a growing (convection and reconnection) and rotating island at $q = 1$, and finite thermal diffusivity across field lines. Sawtooth shapes similar to those observed in the experiment are reproduced when the power deposition location is moved from the magnetic axis to the $q = 1$ region.

The observation that the sawtooth period is at a maximum when the power is deposited close to the $q = 1$ surface has also been reproduced by simulation. The model simulates the evolution of the local magnetic shear and includes a critical shear above which the resistive internal kink is triggered.

The improved understanding of sawtooth behaviour may lead to the capability of controlling sawteeth in tokamaks.

Acknowledgements

This work was partly supported by the Fonds national suisse de la recherche scientifique.

References

[1] Cordey, J.G., et al., Plasma Phys. Control. Fusion **39** (1997) B115.
[2] ITER Global Data Base Working Group, IAEA-CN-69/ITERP1/7, paper presented at 17th IAEA Conf. on Fusion Energy, Yokohama, 1998.
[3] Martin, Y., Sauter, O., Considerations on Energy Confinement Time Scalings using Present Tokamak Databases and Prediction for ITER Size Experiments, Rep. LRP 616/98, Centre de recherches en physique des plasmas, Lausanne.
[4] Miller, R.L., et al., Phys. Rev. Lett. **43** (1979) 765.
[5] Troyon, F., et al., Plasma Phys. Control. Fusion **26** (1984) 209.
[6] Hofmann, F., et al., Phys. Rev. Lett. **81** (1998) 2918.
[7] Lazarus, E.A., et al., Phys. Fluids B **3** (1991) 2220.
[8] Goodman, T.P., et al., in Proc. 19th Symp. on Fusion Technology, Lisbon, 1996 (Varandas, C., Serra, F., Eds), Vol. 1, Elsevier, Amsterdam (1997) 565.
[9] Goodman, T.P., et al., in Proc. 3rd Int. Workshop on Strong Microwaves in Plasmas, Nizhny Novgorod, 1996 (Litvak, A.G., Ed.), Nizhny Novgorod Univ. Press (1997) 35.
[10] Weisen, H., et al., Plasma Phys. Control. Fusion **40** (1998) 1803.
[11] Pochelon, A., et al., in Controlled Fusion and Plasma Physics (Proc. 25th Eur. Conf. Prague, 1998), Vol. 22C, European Physical Society, Geneva (1998) 1324.
[12] Weisen, H., et al., Nucl. Fusion **37** (1997) 1741.
[13] Moret, J.-M., et al., Phys. Rev. Lett. **79** (1997) 2057.
[14] Rebut, P.H., Lallia, P.P., Watkins, M.L., in Plasma Physics and Controlled Nuclear Fusion Research 1988 (Proc. 12th Int. Conf. Nice, 1988), Vol. 2, IAEA, Vienna (1989) 191.
[15] Boucher, D., Rebut, P.H., in Proc. IAEA Tech. Committee Mtg on Advances in Simulation and Modelling of Thermonuclear Plasmas, Montreal, 1992, IAEA, Vienna (1993) 142.
[16] Angioni, C., et al., in Proc. Joint Varenna–Lausanne Int. Workshop on Theory of Fusion Plasmas, 18th Int. School of Plasma Physics, Varenna, 1988 (Connor, J.W., Sindoni, E., Vaclavik, J., Eds), ISSP-18, Editrice Compositori, Bologna (1999) 493; Rep. LRP 617/98, Centre de recherches en physique des plasmas, Lausanne (1998) 15.
[17] Dnestrovskij, Yu.N., et al., Plasma Phys. Rep. **23** (1997) 566.
[18] Pietrzyk, Z.A., et al., Nucl. Fusion **39** (1999) 587.
[19] Pietrzyk, Z.A., et al., in Controlled Fusion and Plasma Physics (Proc. 25th Eur. Conf. Prague, 1998), Vol. 22C, European Physical Society, Geneva (1998) 1328.
[20] Pochelon, A., et al., in Controlled Fusion and Plasma Physics (Proc. 24th Eur. Conf. Berchtesgaden, 1997), Vol. 21A, Part II, European Physical Society, Geneva (1997) 537.
[21] Kislov, D.A., et al., in Controlled Fusion and Plasma Physics (Proc. 22nd Eur. Conf. Bournemouth, 1995), Vol. 19C, Part I, European Physical Society, Geneva (1995) 369.
[22] Razumova, K.A., et al., Plasma Phys. Rep. **23** (1997) 13.
[23] Porcelli, F., et al., Phys. Rev. Lett. **82** (1999) 1458.
[24] Kadomtsev, B.B., Fiz. Plazmy **1** (1975) 710.
[25] Lopes Cardozo, N.J., et al., Phys. Rev. Lett. **73** (1994) 256.
[26] Cima, G., et al., Plasma Phys. Control. Fusion **40**

(1998) 1149.
[27] Porcelli, F., et al., Plasma Phys. Control. Fusion **38** (1996) 2163.
[28] Sauter, O., et al., in Proc. Joint Varenna–Lausanne Int. Workshop on Theory of Fusion Plasmas, 18th Int. School of Plasma Physics, Varenna, 1998 (Connor, J.W., Sindoni, E., Vaclavik, J., Eds), ISSP-18, Editrice Compositori, Bologna (1999) 403; Rep. LRP 617/98, Centre de recherches en physique des plasmas, Lausanne (1998) 49.

(Manuscript received 9 December 1998
Final manuscript accepted 14 April 1999)

E-mail address of A. Pochelon:
Antoine.Pochelon@epfl.ch

Subject classification: F0, Te; F0, Tt; F0, Ti; F1, Te; F1, Ti; C0, Te; C0, Tt; C0, Ti; D2, Te; D2, Tt; D2, Ti; G1, Te; G1, Tt; G1, Ti; G5, Te